Chem

CellPress

Article

14.1% Efficient Monolithically Integrated Solar Flow Battery

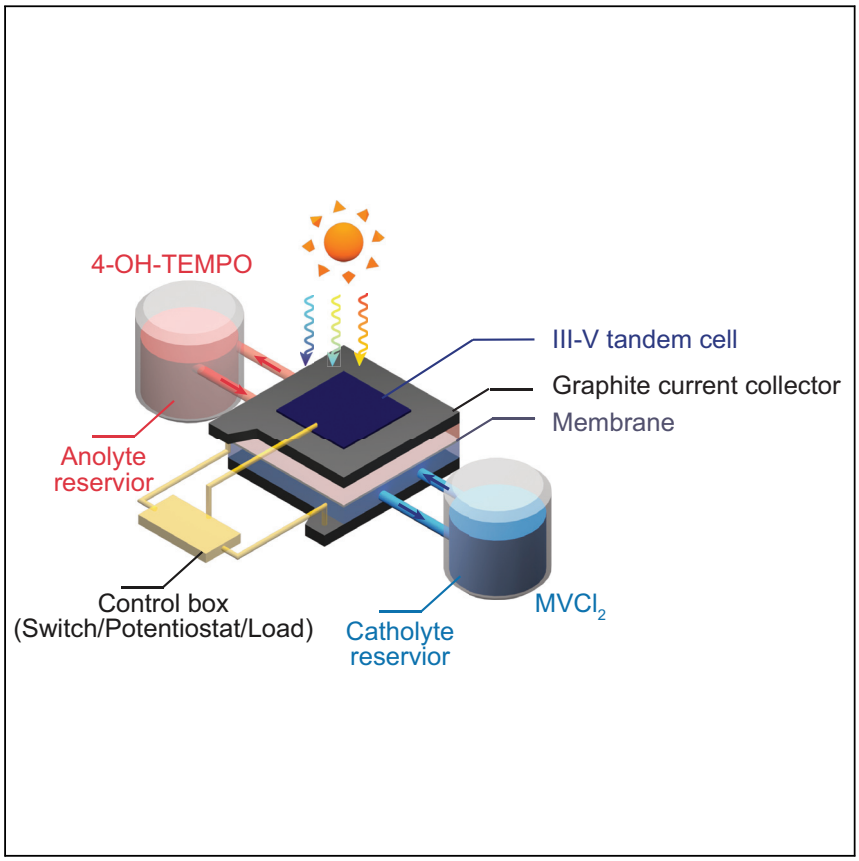

The monolithic integration of photoelectrochemical solar energy conversion and electrochemical energy storage offers an efficient and compact approach toward practical solar energy utilization. This work presents the design principles for and the demonstration of a highly efficient integrated solar flow battery device with a record solar-to-output electricity efficiency. These results will enable a highly efficient approach for practical off-grid solar utilization and electrification.

Wenjie Li, Hui-Chun Fu, Yuzhou Zhao, Jr-Hau He, Song Jin

jin@chem.wisc.edu

HIGHLIGHTS

Monolithic integration of solar energy conversion, storage, and electricity delivery

Record solar-to-output electricity efficiency of 14.1%

General design principles for further development of highly efficient integrated device

Li et al., Chem 4, 1–14
November 8, 2018
https://doi.org/10.1016/j.chempr.2018.08.023

Please cite this article in press as: Li et al., 14.1% Efficient Monolithically Integrated Solar Flow Battery, Chem (2018), https://doi.org/10.1016/j.chempr.2018.08.023

Chem

CellPress

Article

14.1% Efficient Monolithically Integrated Solar Flow Battery

Wenjie Li,[1] Hui-Chun Fu,[2] Yuzhou Zhao,[1] Jr-Hau He,[2] and Song Jin[1,3,*]

SUMMARY

Challenges posed by the intermittency of solar energy source necessitate the integration of solar energy conversion with scalable energy storage systems. The monolithic integration of photoelectrochemical solar energy conversion and electrochemical energy storage offers an efficient and compact approach toward practical solar energy utilization. Here, we present the design principles for and the demonstration of a highly efficient integrated solar flow battery (SFB) device with a record solar-to-output electricity efficiency of 14.1%. Such SFB devices can be configured to perform all the requisite functions from solar energy harvest to electricity redelivery without external bias. Capitalizing on high-efficiency and high-photovoltage tandem III-V photoelectrodes that are properly matched with high-cell-voltage redox flow batteries and carefully designed flow field architecture, we reveal the general design principles for efficient SFBs. These results will enable a highly efficient approach for practical off-grid solar utilization and electrification.

INTRODUCTION

The practical utilization of solar energy demands not only efficient energy conversion but also inexpensive large-scale energy storage to accommodate the intermittency of sunlight.[1] Natural photosynthesis represents a promising approach to efficiently utilize solar energy by converting and storing solar energy in chemical bonds. Studies since the 1970s[2] have shown that artificial photosynthesis can also be accomplished with semiconductors in direct contact with liquid electrolytes to perform photoelectrolysis.[3,4] While much research effort has focused on storing solar energy in molecular fuels by irreversible photoelectrochemical (PEC) reactions, such as PEC water splitting[3,4] and carbon dioxide reduction reaction,[5] the great versatility of semiconductor-based photoelectrolysis also permits reversible redox couples to be used as solar energy storage media.[6,7] Moreover, reversible electrochemical reactions are also exactly what happens during the energy storage process in rechargeable batteries.[8] In this way, the PEC solar energy conversion process can be seamlessly connected with rechargeable batteries by the common reversible redox reactions they share to realize an integrated device that can be directly charged by solar light and discharged like normal batteries when needed.

The concept of the "solar rechargeable battery" was perhaps first demonstrated in 1976 with a polycrystalline CdSe photoelectrode and silver-silver sulfide solid battery electrode.[9] Since then, various approaches toward integrated solar energy conversion and storage have been developed.[10–12] For example, common rechargeable batteries such as lithium-ion batteries,[13] batteries based on other inorganic chemistry,[14] and redox flow batteries (RFBs)[15–21] can be integrated with different types of solar cells. Among these, the integration of PEC cells with RFBs is particularly

The Bigger Picture

Because of the intermittent nature of sunlight, the design of practical round-trip solar energy utilization systems requires both efficient solar energy conversion and storage. Compared with separated solar energy conversion and storage devices, combining the functions of separated devices into a single device allows us to bypass the intermediate step of electricity generation, which represents a more efficient, compact, and cost-effective approach to utilizing solar energy. Here, we present a monolithically integrated solar flow battery device that builds on III-V solar cells and organic redox species. The excellent performance of this device and the general design principles proposed here promise a general approach for storing the intermittent solar energy electrochemically with high storage capacity and efficiency, which will accelerate the large-scale deployment of solar energy technologies, especially in remote locations, to enable practical off-grid electrification.

Please cite this article in press as: Li et al., 14.1% Efficient Monolithically Integrated Solar Flow Battery, Chem (2018), https://doi.org/10.1016/j.chempr.2018.08.023

attractive because of the wide selection of redox couples[22–25] and ease of scaling up the energy storage capacity in RFBs.[26–28] Recently, by integrating silicon solar cells and all-organic quinone-based RFBs, the proof of concept for a bias-free solar energy conversion and electrochemical storage was demonstrated in a solar flow battery (SFB).[29] However, despite the much higher solar conversion efficiency of the silicon solar cells employed, this prototype device could only achieve a modest solar-to-output electricity efficiency (SOEE) of 1.7%, which is not sufficient for practical applications.

This and other examples make it clear that simply integrating high-performance solar cells and RFBs does not necessarily guarantee an SFB with a high SOEE. With comprehensive mechanism study and deeper understanding of the operation principles of SFBs, we now propose a set of design principles for highly efficient integrated SFB devices. Generally, the photoelectrode used for solar energy conversion devices can be categorized into two types, semiconductor-liquid junction cells[30–32] and photovoltaic (PV) cells.[33] For semiconductor-liquid junction cells, energy-level matching between semiconductors and redox species is critical as it determines the photovoltage of such cells.[21] On the other hand, the photovoltage of PV cells is generated by their internal solid-state junctions, and are thus insensitive to the redox potential of the specific redox couple used. By utilizing PV cells the difficulties in the overall device design and voltage matching can be greatly reduced, which makes it a good choice for the purpose of proof-of-principle demonstration. Here, we present a high-efficiency, monolithically integrated SFB device with a record average SOEE of 14.1% and demonstrate that solar energy harvest, conversion, storage, and redelivery can be completed by such a single integrated device without any external electrical energy input. This highly efficient SFB is enabled by high-photovoltage and highly efficient III-V tandem solar cells, carefully matching them with high-voltage RFBs, and dedicatedly designed zero-gap flow field architecture.

RESULTS AND DISCUSSION

SFB Device Design and Operations

Building a highly efficient integrated SFB device starts from designing the general structure of the device, followed by developing and studying the individual components that fit well with the general structure. As illustrated in Figure 1A, we design a simple three-electrode device by incorporating a semiconductor photoelectrode into the conventional two-electrode device design that has been used for most RFBs.[26] Consequently, this device can be operated as a normal RFB with only two carbon felt-based inert electrodes to charge and discharge the redox active species in the liquid electrolytes (Figure 1C), which are constantly circulated between the device and external storage tanks by pumps. More importantly, the charging of this device can also be accomplished by illuminating the photoelectrode with solar light to allow the harvest of photogenerated carriers by redox active species at the semiconductor-liquid electrolyte interface (Figure 1D). We can also operate this device just as a PV solar cell by cycling the redox couples between the photoelectrode and the counter electrode to directly extract the electricity (Figure 1E), which is how regenerative PEC liquid junction solar cells work.[7] To improve the flow dynamics of electrolyte as well as minimize ionic and contact resistance between each component, we configure the new integrated device to allow the membrane, electrode, and current collector to come in direct contact (Figure S1), resembling the zero-gap flow field cell architecture of RFBs.[34]

[1]Department of Chemistry, University of Wisconsin-Madison, 1101 University Avenue, Madison, WI 53706, USA

[2]Division of Computer, Electrical and Mathematical Sciences and Engineering, King Abdullah University of Science and Technology, Thuwal 23955-6900, Saudi Arabia

[3]Lead Contact

*Correspondence: jin@chem.wisc.edu

https://doi.org/10.1016/j.chempr.2018.08.023

Please cite this article in press as: Li et al., 14.1% Efficient Monolithically Integrated Solar Flow Battery, Chem (2018), https://doi.org/10.1016/j.chempr.2018.08.023

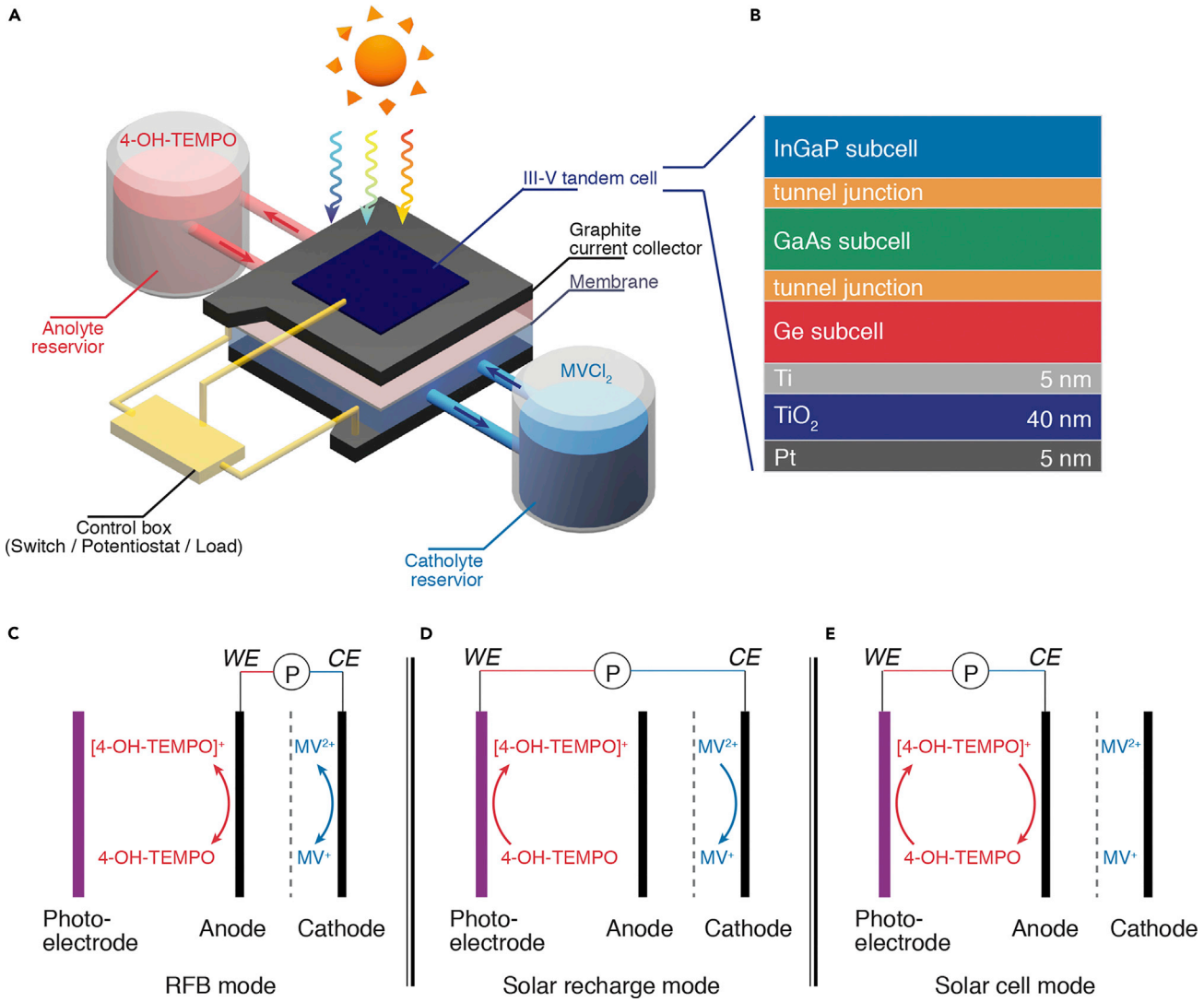

Figure 1. Schematic of SFB Device Design and Operation

(A) Integrated SFB device using III-V tandem cell photoelectrode and 4-OH-TEMPO/$MVCl_2$ redox couples.

(B) Architecture of the photoelectrode based on InGaP/GaAs/Ge tandem solar cell protected by Ti/TiO_2/Pt layers on the surface of the Ge bottom cell.

(C–E) The integrated device configuration under different operation modes: (C) RFB mode, (D) solar recharge mode, and (E) solar cell mode. The definition of anode and cathode follows the charging process.

Electrochemical Characterization of Redox Couples

We chose low-cost organic redox couples 4-hydroxy-2,2,6,6-tetramethylpiperidin-1-oxyl (4-OH-TEMPO) and methyl viologen (MV) as the anolyte and the catholyte, respectively, for the integrated SFB device. By reason of their proper formal potential (E^0) matching, the combination of 4-OH-TEMPO and MV enabled a demonstration of RFBs with an exceptionally high cell voltage of 1.25 V (Figure 2A), which is a significantly high value for aqueous organic RFBs.[35] Although the potential difference between the two redox couples already reach the limit of thermodynamic water-splitting potential (1.23 V), the large overpotentials of water oxidation and reduction reactions on carbon-based electrodes under neutral condition leave at least 400 mV on each side to practically operate the anodic and cathodic redox reactions without electrolysis of water. Given the large E^0 difference between the two

Please cite this article in press as: Li et al., 14.1% Efficient Monolithically Integrated Solar Flow Battery, Chem (2018), https://doi.org/10.1016/j.chempr.2018.08.023

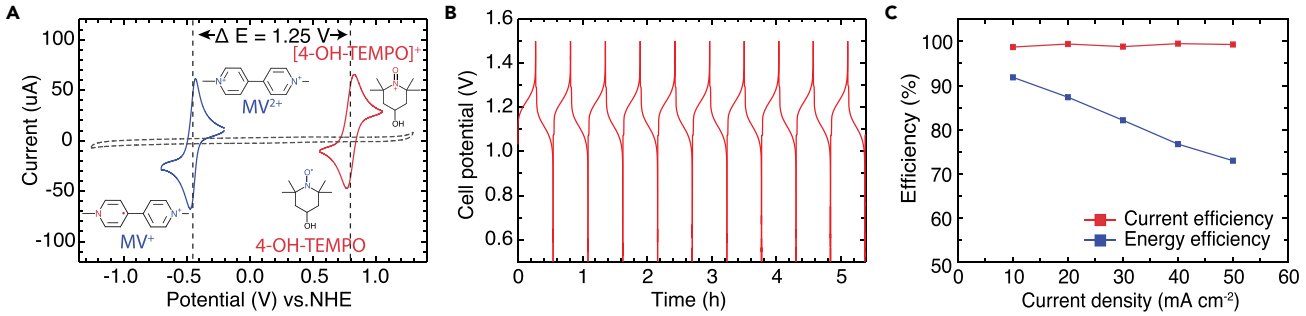

Figure 2. Cyclic Voltammogram and RFB Performance of the 4-OH-TEMPO/MV Redox Couples

(A) Cyclic voltammogram (CV) of 5 mM 4-OH-TEMPO (red curve) and 5 mM $MVCl_2$ (blue curve) in 2 M NaCl scanned at 100 mV s^{-1} on a glassy carbon electrode shows a 1.25 V potential difference. The dotted line represents a CV of 2 M NaCl background electrolyte scanned at 100 mV s^{-1}.

(B) Representative voltage profile during ten charge-discharge cycles of the 0.1 M 4-OH-TEMPO/0.1 M $MVCl_2$ RFB.

(C) RFB current efficiency and energy efficiency at different current densities.

redox couples, we utilized a high-photovoltage triple-junction III-V tandem photoelectrode that consists of an InGaP top cell (E_g = 1.85 eV), a GaAs middle cell (E_g = 1.42 eV), and a Ge bottom cell (E_g = 0.67 eV) (Figure 1B; for more device details see Figure S2).[36] Such monolithic III-V tandem heterojunctions have been proved to be the best for high-efficiency solar cells and furthermore have been shown to be an excellent candidate for PEC water splitting because of their near-ideal band-gap energy and adsorption-spectrum match with solar irradiation.[33,37] Moreover, the III-V tandem cell can provide a high photovoltage (2.4 V) out of a single cell. This high photovoltage, although not specifically critical for PV cells as the panel voltage can be easily increased by series tandem, is a key beneficial feature in integrated SFB device design to enable efficient photocharging of the device without external bias and a simpler three-electrode SFB device design (as shown in Figure 1A). Compared with the four-electrode SFBs previously demonstrated,[29] the three-electrode SFBs are easier to fabricate and operate because only one photoelectrode is needed and illumination comes from one side. Another advantage of these 4-OH-TEMPO and MV redox couples is that they both have relatively large solubility (>0.5 M) in neutral solution; thus, using neutral rather than acidic or alkaline electrolyte greatly reduces the corrosiveness of the electrolyte, and more stable devices readily achieved.

We then studied the redox couples, which serve as the bridge connecting photocharging and electrical discharging processes. The E^0 for 4-OH-TEMPO and MV redox couples are 0.80 V and −0.45 V in 2 M NaCl solution, respectively (Figure 2A). Besides the proper E^0, the electrochemical kinetics and reversibility of the redox couples are also important for the power capability of RFB[27] and even more important for the efficient charge transfer from the semiconductors to electrolytes in PEC devices.[29] Detailed cyclic voltammetry studies at various scan rates (Figure S3) revealed that both redox couples have remarkable electrochemical reversibility and rapid diffusion rate, similar to that of other commonly used fast organic redox couples, such as quinones.[24] Building on the excellent electrochemical properties of the redox couples, we tested the RFB by using 0.1 M 4-OH-TEMPO as anolyte and 0.1 M MV as catholyte, both with 2 M NaCl as supporting electrolyte. The RFB charge-discharge cycling test was carried out in the device shown in Figure S1 at desired constant current density with cutoff voltages of 0.5 and 1.5 V. The representative cycling behavior at 20 mA cm^{-2} (Figure 2B) shows a stable voltage profile over at least ten cycles with an average open-circuit voltage of around 1.2 V. The rate performance study of the RFB at various current densities (Figure 2C) shows that

Please cite this article in press as: Li et al., 14.1% Efficient Monolithically Integrated Solar Flow Battery, Chem (2018), https://doi.org/10.1016/j.chempr.2018.08.023

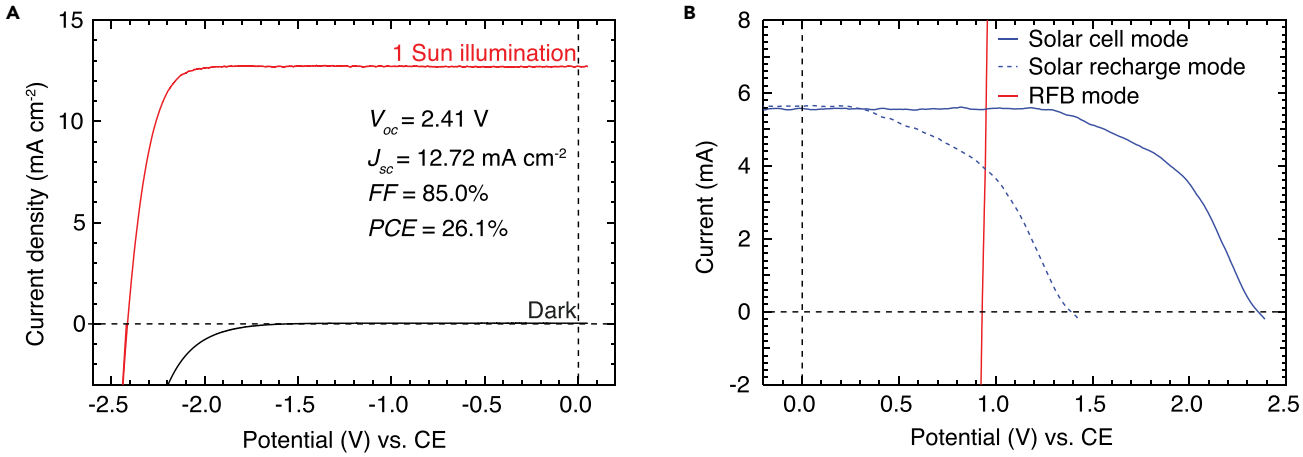

Figure 3. Performance of Individual SFB Components

(A) *J-V* performance of solid-state InGaP/GaAs/Ge tandem solar cell under 1 sun (AM 1.5G) illumination (red) and in the dark (black).

(B) Overlaid *I-V* data for the individually measured photoelectrode and RFB components of the integrated device. Note that current instead of current density is shown here for a photoelectrode with an area of ~0.4 cm^2 and RFB electrodes with an area of 4 cm^2. *J-V* curve for the same photoelectrode is shown in Figure S6. The blue curves represent the PEC solar performance of the III-V tandem photoelectrode measured under solar cell mode (solid) and solar recharge mode (dashed) in 0.1 M 4-OH-TEMPO/0.1 M $MVCl_2$ electrolyte; the red line shows the polarization performance of the 4-OH-TEMPO/$MVCl_2$ RFB. The intersection of the solid blue curve and red line represents the operating point of the SFB device.

the current efficiency (CE) stays at 99% for all the rates while the energy efficiency drops from 91.9% to 73.0% as the rate increases from 10 to 50 mA cm^{-2}. The RFB cycling performance achieved by our SFB device is comparable with that of the previously demonstrated 4-OH-TEMPO/MV RFB,[35] indicating that, although not specifically optimized for RFB performance, the design of this integrated SFB device is competitive with the state-of-the-art RFB architecture.

Performance of Individual SFB Components

We then characterized the performance of the solid-state III-V tandem solar cell under 1 sun (100 mW cm^{-2}) of AM 1.5G simulated solar illumination. The linear sweep voltammetry curve in Figure 3A shows that the solid-state tandem cell exhibits an open-circuit potential (V_{oc}) of 2.41 V, a short-circuit current density (J_{sc}) of 12.72 mA cm^{-2}, a fill factor (FF) of 85.0%, and a power conversion efficiency (PCE) of 26.1%. Previous efforts to use III-V semiconductors in PEC cells showed that III-V semiconductors are very prone to photocorrosion in aqueous electrolytes, especially under extreme pH conditions that are conducive to PEC water electrolysis.[36] Although the neutral electrolyte adopted in our SFB device partially alleviated the corrosive attack by H^+ or OH^- ions, a surface protection layer for the photoelectrode was still required to achieve stable operation. TiO_2 has been widely used as the protection layer and has shown good stability and low charge-transfer resistance in aqueous electrolytes under various pH conditions.[38,39] Therefore, we deposited a Ti/TiO_2 (5/40 nm) thin film on the back side of the III-V cell (Ge bottom cell side) by using sputter coating and atomic layer deposition (ALD) to protect the photoelectrode. A 5 nm layer of Pt was then sputter coated on top of the TiO_2 film to provide a stable ohmic contact between TiO_2 and electrolyte (see Figure 1B).

As illustrated in Figures 1D and 1E, we can configure the integrated SFB device to two different solar modes under illumination. Under solar cell mode (Figure 1E), the photoelectrode and anode are connected to allow photo-oxidation of 4-OH-TEMPO at the surface of photoelectrode and reduction of $[4\text{-OH-TEMPO}]^+$ at the surface of anode, just like regenerative PEC liquid junction solar cells.[7] Thus, the

Please cite this article in press as: Li et al., 14.1% Efficient Monolithically Integrated Solar Flow Battery, Chem (2018), https://doi.org/10.1016/j.chempr.2018.08.023

solar energy input can be directly converted and delivered as electrical energy output to power external load. The PEC performance of the tandem photoelectrode in 0.1 M 4-OH-TEMPO aqueous solution under 1-sun simulated illumination by an EKE-type lamp (solid blue curve in Figure 3B) was very close to the *J-V* performance of the solid-state PV cell (Figure 3A), especially for the V_{oc} and J_{sc}. Note that Figure 3B is displayed in current, not current density, as the areas of photoelectrode (~0.4 cm^2) and the carbon felt RFB electrode (4 cm^2) are different. The lower FF of the photoelectrode (60.3%) in comparison with that of the solid-state cell may be attributed to the mass transport losses of the 4-OH-TEMPO redox couple and the electrolyte ohmic losses between the photoelectrode and anode, which is commonly observed in many PEC cells.[3] In contrast, under solar recharge mode (Figure 1D), the photoelectrode and cathode are connected to drive the photo-oxidation of 4-OH-TEMPO at photoelectrode and simultaneous reduction of MV^{2+} at carbon felt cathode. Solar energy can be harvested by the photoelectrode and stored as chemical energy by the redox reactions under solar recharge mode and released under RFB mode (Figure 1C) as electrical energy when needed. The dashed blue curve in Figure 3B shows the PEC performance of the photoelectrode under solar recharge mode, which can be well matched by cathodically offsetting the solid blue curve. The potential offset between the two PEC *I-V* curves (~1.0 V) comes from the equilibrium potential (E_{eq}) difference between 4-OH-TEMPO and MV redox couples at the specific state of charge (SOC) where the measurements were performed, which agrees well with the open-circuit voltage of the RFB tested at the same SOC (red line in Figure 3B). By overlaying the polarization curve of the RFB and the *I-V* curve of the photoelectrode under solar cell mode, the operation point of the integrated SFB can be found as the intersection of the two curves. From the overlaid *I-V* curves shown in Figure 3B, we can estimate a bias-free solar recharging current of 5.56 mA for the integrated SFB device.

Moreover, we use a specific figure of merit, SOEE, to evaluate the overall efficiency of the SFB device, which is defined as

$$\text{SOEE}\ (\%) = \frac{E_{\text{discharging}}}{E_{\text{illumination}}} = \frac{\int I_{\text{out}} V_{\text{out}} dt}{\int S A dt}, \qquad \text{(Equation 1)}$$

where $E_{\text{discharging}}$ is the usable electrical energy delivered by the integrated SFB device and $E_{\text{illumination}}$ is the total solar energy input.[29] If the RFB polarization curve intersects with the plateau part of the photoelectrode *J-V* curve (see an example in Figure 3B), the SOEE of the integrated device can be estimated with the following equation:

$$\text{estimated SOEE} = \frac{J_{sc}(\text{photo}) \times V_{oc}(\text{RFB}) \times \text{CE} \times \text{VE}}{S}, \qquad \text{(Equation 2)}$$

where J_{sc} (photo) is the short-circuit current density of the photoelectrode, V_{oc}(RFB) is the open-circuit voltage of the RFB, and CE and VE are the estimated current efficiency and voltage efficiency of the SFB. From the data shown in Figure 3B, we can estimate an SOEE of 13.3% for the SFB device (see calculation details in the Experimental Procedures).

Study of Integrated SFB Device

In light of the excellent and reproducible performance of the RFB as well as the good performance from the tandem III-V photoelectrode, we built the integrated SFB devices by using the same RFB and PEC components (Figure S1). The cycling behavior of the SFB was characterized with two potentiostats configured to solar recharge mode and RFB mode to monitor the photocurrent delivered by the photoelectrode

Please cite this article in press as: Li et al., 14.1% Efficient Monolithically Integrated Solar Flow Battery, Chem (2018), https://doi.org/10.1016/j.chempr.2018.08.023

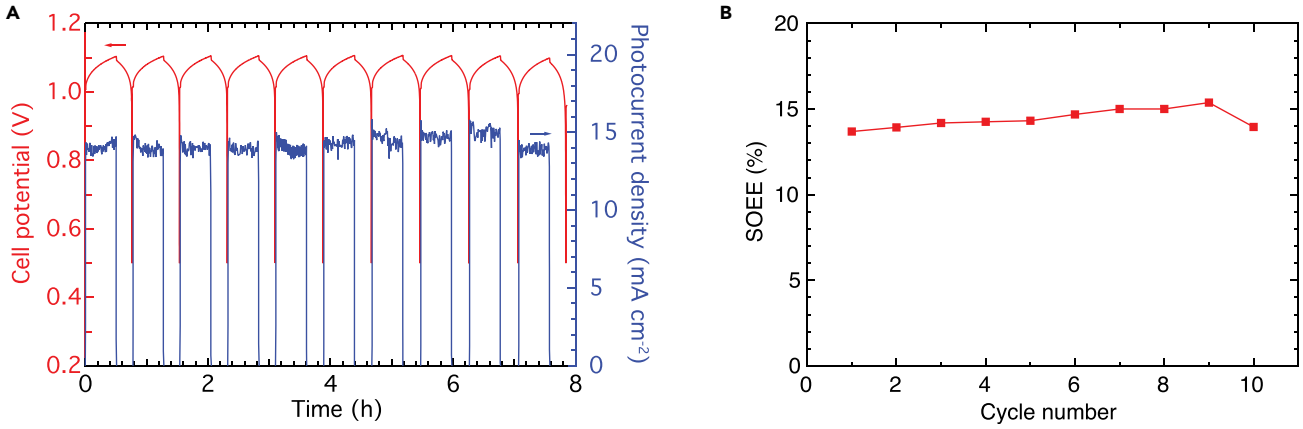

Figure 4. Integrated SFB Device Performance

(A) A representative device cycling behavior showing cell potential between cathode and anode, as well as the photocurrent density delivered by the photoelectrode for ten cycles. The cycling test was performed with no bias potential input during charging process and a current of −10 mA during discharging process.

(B) The SFB displayed a stable SOEE around 14% for ten cycles.

and the cell potential of the integrated SFB device, respectively. The blue curve in Figure 4A shows that the photocurrent density under 1-sun illumination during the unassisted photocharging process stays at 14.5 mA cm^{-2} over ten photocharging cycles with a fluctuation of ± 1 mA cm^{-2} that is likely due to the instability of the light source. After each photocharging cycle, we discharged the device by applying a discharging current of −10 mA until the cell potential reached 0.5 V. The CE and VE of the SFB can be calculated by the same methods used for normal RFBs. Figure S4 shows that the integrated device features both high CE and VE with average efficiencies of 96.2% and 96.6% over ten cycles, respectively. On the basis of the cycling data, we can calculate the actual SOEE for the SFB to directly evaluate its overall efficiency. The integrated SFB device achieved a stable SOEE over ten cycles with an average of 14.1%, which is over 8-fold higher than the prototype device demonstrated previously[29] and the highest published so far among all integrated solar rechargeable battery devices.[10,11] For a broader comparison, the SOEE and other key performance metrics of reported representative SFBs and other solar rechargeable batteries are summarized in Table S1.

Design Principles for Highly Efficient SFB Device

The record SOEE achieved by the integrated SFB device demonstrated here is enabled by the following set of design principles. First, just like the RFBs,[27] for the integrated SFB devices, even with the same photoelectrode and electrolyte, different flow cell structures could result in significantly different device performance and characteristics, especially for the liquid junction photoelectrodes that are more sensitive to the mass transfer rate of redox active species.[40] To accommodate all the components and functions yet maintain a high performance, the SFB device should be dedicatedly designed and optimized. The zero-gap structure of the SFB device employed here only allows a very thin liquid layer (~2 mm) contacting with the photoelectrode, thus ensuring effective diffusion and convection of redox couples at moderate flow rate. More importantly, comparison of the efficiency of the RFB component and solar component clearly shows that here the SOEE is mainly limited by the solar conversion efficiency of the photoelectrode. The photoelectrode used here was fabricated with a triple-junction III-V solar cell that can absorb most of the solar irradiation across the whole solar spectrum to provide a high PCE and,

Please cite this article in press as: Li et al., 14.1% Efficient Monolithically Integrated Solar Flow Battery, Chem (2018), https://doi.org/10.1016/j.chempr.2018.08.023

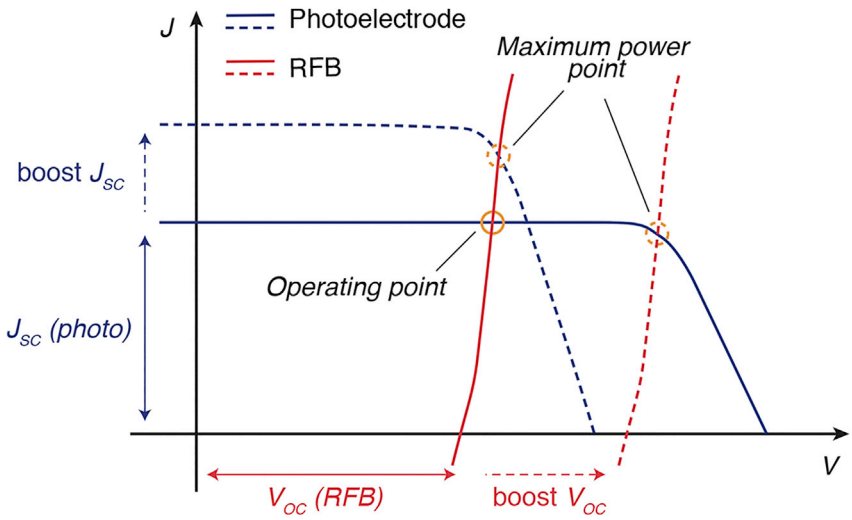

Figure 5. Estimation Method and Pathways to Boost the SOEE of SFB Device

Overlaid hypothetical current-potential behavior for photoelectrodes and RFBs, showing the scenarios of working voltage mismatch (solid curves) and ideal match (dashed curves). The highest SOEE can be achieved by matching the RFB cell voltage with the maximum power point of the photoelectrode. This can be accomplished by either increasing the RFB cell voltage (V_{oc}) to match the given photoelectrode, or boosting the photocurrent density (J_{sc}) of the photoelectrode to match with the given RFB working voltage, allowing the polarization curve of RFB to intersect with the maximum power point of the photoelectrode.

more importantly, a high photovoltage. Lastly, the E^0 difference between the redox couples used in anolyte and catholyte determines the cell voltage of the SFB, which can significantly affect the SOEE (as suggested by Equation 2) as well as the energy and power capacity of the device.

The highly efficient SFB device demonstrated here illustrates the general principles for designing a highly efficient SFB device with the available high-performance solar cells and RFBs: the RFB cell voltage should be matched as closely as possible with the maximum power point of the photoelectrode (Figure 5). In the specific case at hand, the 4-OH-TEMPO/MV redox couple combination boasts one of the highest cell voltages (1.25 V) among the aqueous organic RFBs demonstrated so far, which is a great boost for the SOEE. To drive the unassisted photocharging of SFBs with such a high cell voltage, the V_{oc} produced by the photoelectrode needs to be at least 1.4 V to compensate for the inevitable voltage losses. Therefore, V_{oc} higher than 1.8 V is generally not useful for driving the 4-OH-TEMPO/MV redox reactions. This means that an excess photovoltage of around 0.6 V produced herein by the tandem III-V photoelectrode was not contributing to the SOEE. This voltage mismatch is the most significant reason for the efficiency loss from the PCE of the solar cells to the final SOEE. As illustrated in Figure 5, if an RFB with an even higher cell voltage can be employed to shift the solid red RFB polarization curve to the hypothetical dashed red curve, it can not only improve the SOEE but also raise the energy density of the SFB. Therefore, there is still much untapped potential in the tandem III-V photoelectrode to further increase the SOEE of SFBs. With many new and emerging redox couples that are being developed for RFBs,[22–28] such as the one reported recently,[41] this strategy promises a clear pathway for future developments. Moreover, not only is high (photo)voltage highly desirable for both the RFBs and the photoelectrodes used in SFBs, but properly matching their voltages is also the critical factor for taking advantage of such high-efficiency solar cells to enable the highest SOEE out of the

Please cite this article in press as: Li et al., 14.1% Efficient Monolithically Integrated Solar Flow Battery, Chem (2018), https://doi.org/10.1016/j.chempr.2018.08.023

integrated SFBs. An alternative strategy for improving voltage matching could be boosting the J_{sc} of the photoelectrode, which is usually accompanied by some sacrifice in the photovoltage (from solid blue to dashed blue curve in Figure 5); however, as long as the photovoltage is still higher than the RFB cell voltage, we can still achieve intersection at maximum power point. Such a design would involve tuning the band structures of the tandem III-V photoelectrodes or integrating other materials into tandem double junctions,[42] therefore making it more complicated.

Because of the expensive III-V substrates and heteroepitaxial growth, the manufacturing cost for tandem III-V photoelectrodes may be too high to be employed for practical applications. At this early stage of the development of SFBs, we are trying to demonstrate the design principles and push the boundaries to show what could be possibly achieved, with some sacrifice regarding cost effectiveness. However, the cost of III-V cells may be reduced in the future by designing simpler tandem cells with a sufficiently high photovoltage[42] or adopting new fabrication methods, such as epitaxial liftoff.[43] With further developments and proper device design following the design principles laid out herein, we believe that the capital cost for monolithically integrated SFB devices will not be higher than individually operated PV devices plus RFBs. Furthermore, developing new semiconductor materials[30] and incorporating them into more efficient liquid junction cells[7,31,32] could further simplify the SFB photoelectrode fabrication process and lower the cost.

Conclusion

In conclusion, building on novel device design and a set of rational design principles, we demonstrated a high-performance monolithic solar energy conversion and storage device by using highly efficient and high-photovoltage tandem III-V solar cells and high-voltage 4-OH-TEMPO/MV RFBs. The integrated SFB device can be easily configured to three different operation modes to fit specific application requirements. Enabled by a high-efficiency photoelectrode, properly matched redox couples, and carefully designed flow field design, a record SOEE of 14.1% has been achieved for the SFB. Following the design rules proposed herein, the efficiency of such SFB devices in general could be further boosted by better voltage matching of the RFBs and solar cells either by enlarging the RFB cell potential with better redox couple choices or by tuning the band structure of solar cells to improve its J_{sc}. This work paves the way for a practical new approach to harvesting, storing, and utilizing the intermittent solar energy with unprecedented high energy conversion efficiency and energy storage density. These integrated SFBs will be especially suitable as distributed and stand-alone solar energy conversion and storage systems in remote locations and will enable practical off-grid electrification.

EXPERIMENTAL PROCEDURES

Fabrication of RFB and Integrated SFB Device

The RFB and SFB measurements were carried out in a custom-made zero-gap device (Figure S1). Two end frames and two hose adaptor frames were machined out of solid stainless steel and solid PVDF blocks, respectively. Current collectors were 45 × 45 mm^2 graphite plates (1/8 in thickness) with a 20 × 20 × 1.2 mm pocket to place carbon felt electrodes. Current collectors with additional 10 × 10 mm clearance window at the center of the square pocket were used for SFB devices (only on the anode side) to allow direct contact between photoelectrode and liquid electrolyte. Carbon felt electrodes (4 cm^2; GFD 3 EA, SIGRACELL) were pretreated at 400°C in air for 6 hr before being used on both sides of the cell. FAA-3-50 membrane (Fumatech) was used as an anion-exchange membrane, which was soaked in 1 M NaCl for 24 hr before use. The cell was assembled with four pieces of PTFE (0.04 in thickness) sheets

Please cite this article in press as: Li et al., 14.1% Efficient Monolithically Integrated Solar Flow Battery, Chem (2018), https://doi.org/10.1016/j.chempr.2018.08.023

as gaskets and tightened with eight #10-24 bolts torqued to 4.0 Nm. A 20 mL solution of 0.1 M 4-hydroxy-2,2,6,6-tetramethylpiperidin-1-oxyl (4-OH-TEMPO, AK Scientific) in 2 M NaCl (Sigma-Aldrich) and a 10 mL solution of 0.1 M 1,1′-dimethyl-4,4′-bipyridinium dichloride ($MVCl_2$, Fisher Scientific) in 2 M NaCl were used as anolyte and catholyte, respectively. (Note that $MVCl_2$ is toxic and should be carefully handled to avoid releasing to the environment.) The electrolytes were pumped via Viton tubing through the flow channels at a rate of 20 mL min^{-1} by a peristaltic pump (Cole-Parmer Masterflex L/S). All RFB and SFB measurements were carried out in a custom modified N_2 flush box (Terra Universal) with continuous N_2 flushing.

Electrochemical Measurements

Cyclic voltammogram measurements (Figures 2A and S3) were conducted with a Bio-Logic SP-200 potentiostat. A 3 mm diameter glassy carbon disk electrode (BASi) was used as the working electrode, which was polished with 0.3 and 0.05 μm alumina slurry to mirror shine and washed with deionized water (Milli-Q, 18.2 MΩ cm) and methanol before each test. A Pt wire electrode (CH Instruments) and a saturated calomel electrode (SCE, CH Instruments) were used as the counter and reference electrodes, respectively. 4-OH-TEMPO and $MVCl_2$ were used as received to prepare a 5 mM solution of each redox couple with 2 M NaCl as supporting electrolyte. The peak current versus the square root of the scan rate (v) are plotted in Figures S3C and S3D and fitted with a straight line. The Randles-Sevèik equation $i_p = 2.69 \times 10^5 n^{3/2} D^{1/2} c v^{1/2} A$, where number of electrons involved in the electrochemical reaction $n = 1$, $MVCl_2$ and 4-OH-TEMPO concentration $c = 5 \times 10^{-6}$ mol cm^{-3}, and electrode area $A = 0.0707$ cm^2, was used to calculate the diffusion coefficient (D) of the redox couples from the slope of the fitted line. This yields $D_R = 6.53 \times 10^{-6}$ cm^2 s^{-1} and $D_O = 3.31 \times 10^{-6}$ cm^2 s^{-1} for $MVCl_2$ redox couples, and $D_R = 4.14 \times 10^{-6}$ cm^2 s^{-1} and $D_O = 4.12 \times 10^{-6}$ cm^2 s^{-1} for 4-OH-TEMPO redox couples.

RFB Measurements

The RFB cycling and polarization performance tests were carried out with a Bio-Logic SP-200 potentiostat. The RFB cycling tests were performed by charging and discharging the battery at a desired constant current density with 0.5 and 1.5 V as bottom and top potential limits, respectively. In the cell polarization characterization, a linear sweep voltammetry (LSV) scan was performed at a scan rate of 100 mV s^{-1}. Potentiostatic electrochemical impedance spectroscopy measurement of the RFB was performed at 0 SOC, 1.0 V bias with a voltage offset of 10 mV, and frequencies ranging from 200 kHz to 1 Hz (Figure S5).

Fabrication of InGaP/GaAs/Ge Tandem-Junction Solar Cells Coated with Thin-Film Protection Layers

The GaInP/GaAs/Ge triple-junction solar cell consists of an n/p GaInP junction top cell (E_g = 1.80 eV), an n/p GaAs junction middle cell (E_g = 1.42 eV), and an n/p Ge junction bottom cell (E_g = 0.66 eV). Before the growth process, a p-type [100]-oriented germanium substrate was chemically cleaned. After the cleaning process, III-V layer structures were deposited on Ge substrate by metalorganic chemical vapor deposition. Trimethyl gallium (TMGa), trimethyl aluminum (TMAl), and trimethyl indium (TMIn) were used as the sources for the Group-III elements; arsine (AsH_3) and phosphine (PH_3) were used as the source gases for the Group-V elements. Silane (SiH_4) was used as the source of donor impurity, while the sources of acceptor impurities were diethyl zinc (DEZn) and bis-cyclopentadiethyl magnesium (Cp_2Mg).

As illustrated in Figure S2A, the Ge bottom cell was formed by a 150 μm p-Ge base layer, a 300 nm n-Ge emitter, and a 25 nm n-GaInP window layer. The GaAs middle

Please cite this article in press as: Li et al., 14.1% Efficient Monolithically Integrated Solar Flow Battery, Chem (2018), https://doi.org/10.1016/j.chempr.2018.08.023

cell was formed by a 30 nm p-AlGaAs back surface field (BSF) layer, a 25 μm p-GaAs base layer, a 100 nm n-GaAs emitter, and a 100 nm n-AlInP window layer. The GaInP top cell was formed by a 50 nm p-AlGaAs BSF layer, a 6,700 nm p-GaInP base layer, a 30 nm n-GaInP emitter, and a 30 nm n-AlGaAs window layer. The tunnel junction consisting of a 10 nm n^{++}-AlGaAs layer and a 10 nm p^{++}-AlGaAs layer was used to connect each subcell. The thickness of the subcell was confirmed by a cross-section scanning electron microscopy image (Figure S2B).

A dual-layered SiO_2/TiO_2 antireflection coating (7 nm) was evaporated on the top side of the triple-junction device followed by a top metal contact grid (10 nm Ti and 90 nm Au) realized by photo-lithography and e-beam evaporation. A Ge/Au eutectic layer was deposited on the back side of Ge wafer to form ohmic contact. For making the photoelectrodes to be used in the integrated SFBs, a thin (5 nm) layer of titanium was first sputter coated and followed by a 40-nm-thick layer of TiO_2 thin film deposited by ALD using tetrakis(dimethylamino) titanium and O_2-plasma precursors at 150°C in ~200 mTorr Ar environment on the back side of the triple-junction device. On top of that, another layer of 5-nm-thick platinum thin film was sputter deposited to minimize the charge extraction barrier. All of the sputter coatings were carried out by a DC magnetron sputtering method with a power of 400 W.

Fabrication of Photoelectrode Assembly for the Integrated SFB Device

The photoelectrode assembly for the integrated SFB device characterization was fabricated by affixing the III-V tandem cell photoelectrode described above onto a custom-made graphite current collector (described in the SFB device fabrication section) by epoxy resin (Hysol 9460) to cover the window of the current collector. The back side of the III-V cell (Ge side) was only physically attached to the current collector without forming an electrical contact. The 4-OH-TEMPO electrolyte can directly contact with the back side of the III-V cell through the window of the current collector and harvest photogenerated holes during SFB device operation in solar recharge mode and solar cell mode. The ohmic contact to III-V photoelectrode was made by attaching a copper foil onto the front side of the cell (InGaP side) with Ga/In eutectic mixture (Sigma-Aldrich) and fixed with silver paint (Ted Pella, PELCO colloidal silver). The ohmic contact area was sealed by epoxy resin. The geometric area of the exposed III-V cell was determined with calibrated digital images and Photoshop, which was usually between 0.35 and 0.5 cm^2.

Solid-State and Photoelectrochemical Characterization of the III-V Tandem Cells

Solid-state *J-V* performance of the III-V cells was measured in a two-electrode configuration by making ohmic contact to the front and back side of the cell. The data were collected with a Bio-Logic SP-200 potentiostat under 1 sun (100 mW cm^{-2}) of AM 1.5G simulated illumination by a Newport Model 91191 solar simulator. A Si photodiode (Thorlabs) was used to calibrate the illumination intensity of the AM 1.5G solar simulator to 100 mW cm^{-2}.

The PEC characteristics of the III-V tandem photoelectrode were measured in the assembled SFB device with a Bio-Logic SP-200 potentiostat under 1 sun (100 mW cm^{-2}) of simulated solar illumination by an EKE-type tungsten-halogen lamp (USHIO) in a N_2 flush box. For calibration of the EKE-type solar simulator, the short-circuit current of a solid-state p^+nn^+ Si solar cell (~1.2 cm^2) was first measured under 1 sun of AM 1.5G simulated solar light, and then the EKE-type solar simulator was calibrated to generate the same short-circuit current with the same solid-state p^+nn^+ Si solar cell. The PEC measurements were performed

Please cite this article in press as: Li et al., 14.1% Efficient Monolithically Integrated Solar Flow Battery, Chem (2018), https://doi.org/10.1016/j.chempr.2018.08.023

in a two-electrode configuration under both solar cell mode and solar recharge mode (Figures 1D and 1E) with the same electrolytes used in the RFB test (0.1 M 4-OH-TEMPO as anolyte and 0.1 M $MVCl_2$ as catholyte, both with 2 M NaCl as supporting electrolyte). All LSV curves were measured at a scan rate of 100 mV s^{-1} without correcting for any uncompensated resistance losses.

Integrated SFB Device Characterization

To characterize the charging-discharging behaviors of the integrated SFB devices, we used two Bio-Logic SP-200 potentiostats: we configured potentiostat 1 as solar recharge mode (Figure 1D) to monitor the photocurrent and configured potentiostat 2 as RFB mode (Figure 1C) to monitor the potential difference between the two electrodes. During the photocharging process, III-V photoelectrode was illuminated by the EKE-type simulated solar illumination at 1 sun without applying any external bias by potentiostat 1. During the discharging process, the illumination was turned off and the integrated device was operated as a normal RFB with a discharging current of −10 mA applied by potentiostat 2 until the cell potential reached 0.5 V.

The PEC characteristics of the photoelectrodes used in the SFB devices were examined before and after integrated device cycling test according to the methods described in the previous section to check the stability of the III-V photoelectrodes (Figure S6).

Calculation of Solar-to-Output Electricity Efficiency

Because electricity is not directly extracted from the solar conversion device in integrated SFBs, the conventional PCE used to evaluate solar PV cells is not the most suitable metrics. To quantitatively evaluate the solar conversion efficiency of the integrated device, a new figure of merit for this type of integrated SFB devices should be considered, namely SOEE, which is defined by the ratio of the usable electrical energy delivered by the integrated SFB device ($E_{discharging}$) over the total solar energy input ($E_{illumination}$). The SOEE can be calculated with Equation 1:

$$\text{SOEE}\ (\%) = \frac{E_{discharging}}{E_{illumination}} = \frac{\int I_{out} V_{out} dt}{\int S A dt},$$

where I_{out} is the output (discharging) current, V_{out} is the output voltage, S is the total incident solar irradiance, which is provided by the EKE-type light source at 100 mW cm^{-2}, and A is the illumination area of photoelectrode. Note that this SOEE is the round-trip efficiency of the delivered electrical energy over the original solar energy input. If we compare with PEC water splitting, this SOEE is equivalent to the total efficiency after considering both the solar-to-hydrogen conversion efficiency of PEC water-splitting device and the efficiency of the fuel cell that generates electricity from the hydrogen fuel.

If the RFB polarization curve intersects with the plateau part of the PEC *J-V* curve (Figure 5), then the SOEE of the integrated device can be estimated with Equation 2:

$$\begin{aligned}\text{estimated SOEE} &= \frac{J_{sc}(\text{photo}) \times V_{oc}(\text{RFB}) \times \text{CE} \times \text{VE}}{S} \\ &\approx \frac{J_{sc}(\text{photo}) \times V_{oc}(\text{photo}) \times \text{FF} \times V_{oc}(\text{RFB})}{S \times V_{oc}(\text{photo}) \times \text{FF}} \times \text{CE} \\ &\times \text{VE} = \frac{\eta(\text{photo})}{\text{FF}} \times \frac{V_{oc}(\text{RFB})}{V_{oc}(\text{photo})} \times \text{CE} \times \text{VE},\end{aligned}$$

where J_{sc}(photo) is the short-circuit current density of the photoelectrode, V_{oc}(RFB) is the open-circuit voltage of the RFB, CE and VE are the current

efficiency and voltage efficiency of the RFB operated under similar conditions (same charging current, charging time, and potential limits; Figure S7), S is the total incident solar irradiance, V_{oc}(photo) is the open-circuit potential of the photoelectrode, FF is the fill factor of the photoelectrode, and η(photo) is the PCE of the photoelectrode:

$$\text{estimated SOEE} = \frac{\eta\,(\text{photo})}{\text{FF}} \times \frac{V_{oc}(\text{RFB})}{V_{oc}(\text{photo})} \times \text{CE} \times \text{VE}$$

$$= \frac{20.6\%}{60.3\%} \times \frac{1.01\ \text{V}}{2.36\ \text{V}} \times 95.5\% \times 95.6\% = 13.3\%.$$

SUPPLEMENTAL INFORMATION

Supplemental Information includes seven figures and one table and can be found with this article online at https://doi.org/10.1016/j.chempr.2018.08.023.

ACKNOWLEDGMENTS

This research was supported by the King Abdullah University of Science and Technology (KAUST) Office of Sponsored Research under award no. OSR-2017-CRG6-3453.02. H.-C.F. and J.-H.H. are supported by the KAUST baseline fund for the design and fabrication of III-V tandem junction solar cells.

AUTHOR CONTRIBUTIONS

W.L. and S.J. designed the experiments. W.L. fabricated the SFB devices and carried out the electrochemical measurements. H.-C.F. and J.-H.H. fabricated the III-V tandem junction solar cells. Y.Z. and H.-C.F. performed scanning electron microscopy imaging. W.L. and S.J. wrote the manuscript, and all authors commented on the manuscript.

DECLARATION OF INTERESTS

The authors declare no competing interests.

Received: July 17, 2018
Revised: August 16, 2018
Accepted: August 20, 2018
Published: September 27, 2018

REFERENCES AND NOTES

1. Lewis, N.S. (2016). Research opportunities to advance solar energy utilization. Science *351*, aad1920.

2. Honda, K., and Fujishima, A. (1972). Photolysis-decomposition of water at the surface of an irradiated semiconductor. Nature *238*, 37–38.

3. Walter, M.G., Warren, E.L., McKone, J.R., Boettcher, S.W., Mi, Q., Santori, E.A., and Lewis, N.S. (2010). Solar water splitting cells. Chem. Rev. *110*, 6446–6473.

4. Nocera, D.G. (2012). The artificial leaf. Acc. Chem. Res. *45*, 767–776.

5. Montoya, J.H., Seitz, L.C., Chakthranont, P., Vojvodic, A., Jaramillo, T.F., and Norskov, J.K. (2017). Materials for solar fuels and chemicals. Nat. Mater. *16*, 70–81.

6. Luttmer, J.D., Konrad, D., and Trachtenberg, I. (1985). Electrode materials for hydrobromic acid electrolysis in Texas-Instruments solar chemical converter. J. Electrochem. Soc. *132*, 1054–1058.

7. Heller, A., Miller, B., and Thiel, F.A. (1981). 11.5% solar conversion efficiency in the photocathodically protected *p*-InP/V^{3+}-V^{2+}-HCl/C semiconductor liquid junction cell. Appl. Phys. Lett. *38*, 282–284.

8. Yang, Z., Zhang, J., Kintner-Meyer, M.C.W., Lu, X., Choi, D., Lemmon, J.P., and Liu, J. (2011). Electrochemical energy storage for green grid. Chem. Rev. *111*, 3577–3613.

9. Hodes, G., Manassen, J., and Cahen, D. (1976). Photoelectrochemical energy conversion and storage using polycrystalline chalcogenide electrodes. Nature *261*, 403–404.

10. Schmidt, D., Hager, M.D., and Schubert, U.S. (2015). Photo-rechargeable electric energy storage systems. Adv. Energy Mater. *6*, 1500369.

11. Yu, M., McCulloch, W.D., Huang, Z., Trang, B.B., Lu, J., Amine, K., and Wu, Y. (2016). Solar-powered electrochemical energy storage: an alternative to solar fuels. J. Mater. Chem. A *4*, 2766–2782.

12. Gurung, A., and Qiao, Q. (2018). Solar charging batteries: advances, challenges, and opportunities. Joule *2*, 1–14.

13. Paolella, A., Faure, C., Bertoni, G., Marras, S., Guerfi, A., Darwiche, A., Hovington, P., Commarieu, B., Wang, Z., Prato, M., et al. (2017). Light-assisted delithiation of lithium iron phosphate nanocrystals towards photo-rechargeable lithium ion batteries. Nat. Commun. *8*, 14643.

14. Licht, S., Hodes, G., Tenne, R., and Manassen, J. (1987). A light-variation insensitive high efficiency solar cell. Nature *326*, 863–864.

15. Cheng, Q., Fan, W., He, Y., Ma, P., Vanka, S., Fan, S., Mi, Z., and Wang, D. (2017). Photorechargeable high voltage redox battery

enabled by Ta_3N_5 and GaN/Si dual-photoelectrode. Adv. Mater. *351*, 1700312–1700318.

16. Yu, M., McCulloch, W.D., Beauchamp, D.R., Huang, Z., Ren, X., and Wu, Y. (2015). Aqueous lithium-iodine solar flow battery for the simultaneous conversion and storage of solar energy. J. Am. Chem. Soc. *137*, 8332–8335.

17. Liao, S., Zong, X., Seger, B., Pedersen, T., Yao, T., Ding, C., Shi, J., Chen, J., and Li, C. (2016). Integrating a dual-silicon photoelectrochemical cell into a redox flow battery for unassisted photocharging. Nat. Commun. *7*, 11474–11478.

18. Wedege, K., Azevedo, J., Khataee, A., Bentien, A., and Mendes, A. (2016). Direct solar charging of an organic-inorganic, stable, and aqueous alkaline redox flow battery with a hematite photoanode. Angew. Chem. Int. Ed. *55*, 7142–7147.

19. Liu, P., Cao, Y.l., Li, G.R., Gao, X.P., Ai, X.P., and Yang, H.X. (2013). A solar rechargeable flow battery based on photoregeneration of two soluble redox couples. ChemSusChem *6*, 802–806.

20. Wedege, K., Bae, D., Dražević, E., Mendes, A., Vesborg, P.C.K., and Bentien, A. (2018). Unbiased, complete solar charging of a neutral flow battery by a single Si photocathode. RSC Adv. *8*, 6331–6340.

21. Zhou, Y., Zhang, S., Ding, Y., Zhang, L., Zhang, C., Zhang, X., Zhao, Y., and Yu, G. (2018). Efficient solar energy harvesting and storage through a robust photocatalyst driving reversible redox reactions. Adv. Mater. *103*, 1802294–1802297.

22. Ding, Y., Li, Y.F., and Yu, G.H. (2016). Exploring bio-inspired quinone-based organic redox flow batteries: a combined experimental and computational study. Chem *1*, 790–801.

23. Ding, Y., and Yu, G. (2016). A bio-inspired, heavy-metal-free, dual-electrolyte liquid battery towards sustainable energy storage. Angew. Chem. Int. Ed. *55*, 4772–4776.

24. Huskinson, B., Marshak, M.P., Suh, C., Er, S., Gerhardt, M.R., Galvin, C.J., Chen, X., Aspuru-Guzik, A., Gordon, R.G., and Aziz, M.J. (2014). A metal-free organic-inorganic aqueous flow battery. Nature *505*, 195–198.

25. Kwabi, D.G., Lin, K., Ji, Y., Kerr, E.F., Goulet, M.-A., De Porcellinis, D., Tabor, D.P., Pollack, D.A., Aspuru-Guzik, A., Gordon, R.G., et al. (2018). Alkaline quinone flow battery with long lifetime at pH 12. Joule *2*, https://doi.org/10.1016/j.joule.2018.07.005.

26. Park, M., Ryu, J., Wang, W., and Cho, J. (2016). Material design and engineering of next-generation flow-battery technologies. Nat. Rev. Mater. *2*, 16080.

27. Weber, A.Z., Mench, M.M., Meyers, J.P., Ross, P.N., Gostick, J.T., and Liu, Q. (2011). Redox flow batteries: a review. J. Appl. Electrochem. *41*, 1137–1164.

28. Ding, Y., Zhang, C., Zhang, L., Zhou, Y., and Yu, G. (2018). Molecular engineering of organic electroactive materials for redox flow batteries. Chem. Soc. Rev. *47*, 69–103.

29. Li, W., Fu, H.-C., Li, L., Caban-Acevedo, M., He, J.-H., and Jin, S. (2016). Integrated photoelectrochemical solar energy conversion and organic redox flow battery devices. Angew. Chem. Int. Ed. *55*, 13104–13108.

30. Sivula, K., and van de Krol, R. (2016). Semiconducting materials for photoelectrochemical energy conversion. Nat. Rev. Mater. *1*, 15010.

31. Cha, H.G., and Choi, K.S. (2015). Combined biomass valorization and hydrogen production in a photoelectrochemical cell. Nat. Chem. *7*, 328–333.

32. Kamat, P.V., Tvrdy, K., Baker, D.R., and Radich, J.G. (2010). Beyond photovoltaics: semiconductor nanoarchitectures for liquid-junction solar cells. Chem. Rev. *110*, 6664–6688.

33. Khaselev, O., and Turner, J.A. (1998). A monolithic photovoltaic-photoelectrochemical device for hydrogen production via water splitting. Science *280*, 425–427.

34. Aaron, D.S., Liu, Q., Tang, Z., Grim, G.M., Papandrew, A.B., Turhan, A., Zawodzinski, T.A., and Mench, M.M. (2012). Dramatic performance gains in vanadium redox flow batteries through modified cell architecture. J. Power Sources *206*, 450–453.

35. Liu, T., Wei, X., Nie, Z., Sprenkle, V., and Wang, W. (2015). A total organic aqueous redox flow battery employing a low cost and sustainable methyl viologen anolyte and 4-HO-TEMPO catholyte. Adv. Energy Mater. *6*, 1501449.

36. Huang, C.-W., Liao, C.-H., Wu, C.-H., and Wu, J.C.S. (2012). Photocatalytic water splitting to produce hydrogen using multi-junction solar cell with different deposited thin films. Sol. Energy Mater. Sol. Cells *107*, 322–328.

37. Verlage, E., Hu, S., Liu, R., Jones, R.J.R., Sun, K., Xiang, C., Lewis, N.S., and Atwater, H.A. (2015). A monolithically integrated, intrinsically safe, 10% efficient, solar-driven water-splitting system based on active, stable earth-abundant electrocatalysts in conjunction with tandem III-V light absorbers protected by amorphous TiO_2 films. Energy Environ. Sci. *8*, 3166–3172.

38. Mei, B., Pedersen, T., Malacrida, P., Bae, D., Frydendal, R., Hansen, O., Vesborg, P.C.K., Seger, B., and Chorkendorff, I. (2015). Crystalline TiO_2: a generic and effective electron-conducting protection layer for photoanodes and -cathodes. J. Phys. Chem. C *119*, 15019–15027.

39. Hu, S., Shaner, M.R., Beardslee, J.A., Lichterman, M., Brunschwig, B.S., and Lewis, N.S. (2014). Amorphous TiO_2 coatings stabilize Si, GaAs, and GaP photoanodes for efficient water oxidation. Science *344*, 1005–1009.

40. Gibbons, J.F., Cogan, G.W., Gronet, C.M., and Lewis, N.S. (1984). A 14% efficient nonaqueous semiconductor/liquid junction solar cell. Appl. Phys. Lett. *45*, 1095.

41. DeBruler, C., Hu, B., Moss, J., Liu, X., Luo, J., Sun, Y., and Liu, T.L. (2017). Designer two-electron storage viologen anolyte materials for neutral aqueous organic redox flow batteries. Chem *3*, 961–978.

42. Vaisman, M., Fan, S.Z., Yaung, K.N., Perl, E., Martin-Martin, D., Yu, Z.S.J., Leilaeioun, M., Holman, Z.C., and Lee, M.L. (2017). 15.3%-Efficient GaAsP solar cells on GaP/Si templates. ACS Energy Lett. *2*, 1911–1918.

43. Ward, J.S., Remo, T., Horowitz, K., Woodhouse, M., Sopori, B., VanSant, K., and Basore, P. (2016). Techno-economic analysis of three different substrate removal and reuse strategies for III-V solar cells. Prog. Photovolt. *24*, 1284–1292.